Catalysis Science & Technology



PAPER

View Article Online
View Journal | View Issue



Cite this: Catal. Sci. Technol., 2022, 12, 976

Jessica A. Muhlenkamp,^a Nicole J. LiBretto,^b Jeffrey T. Miller ^D and Jason C. Hicks ^{**}

phosphide nanoparticles†

A series of Co–P materials with varying P:Co ratio from 0 to 4 supported on SBA-15 were evaluated for ethane dehydrogenation (EDH) performance. In comparison to monometallic Co, the Co–P materials have improved ethylene selectivity from 41% for Co to 88–90% for Co–P, which was attributed to the segregation of Co atoms and the formation of partial positive $Co^{\delta+}$ sites in the Co–P materials due to charge transfer. Among the Co–P materials studied, an optimum in stability was observed in those containing a P:Co ratio in the range 1 to 2. Below this range, limited P is available to adequately separate Co atoms. Above this range, the excess P promotes coke formation through possible acid catalyzed pathways. The stability of two of the Co–P materials containing the Co₂P and CoP phase, respectively, were further tested for EDH at 700 °C. Under these conditions, the ethylene selectivity was 98%, and both materials remained active with little to no deactivation for over 4 h. In comparison to a Pt–Sn reference, both Co–P materials showed vastly improved stability. Additionally, both Co–P materials showed no signs of sintering after EDH at 700 °C and maintained their respective Co₂P and CoP phases. These results demonstrate the catalytic improvement with P incorporation and highlights the high stability of Co–P, and possibly other metal phosphides, as high temperature EDH catalysts.

Ethane dehydrogenation performance and high

temperature stability of silica supported cobalt

Received 24th September 2021, Accepted 29th December 2021

DOI: 10.1039/d1cy01737c

rsc.li/catalysis

1. Introduction

The growing production of light alkanes from shale gas over the past decade has bolstered interest in the catalytic dehydrogenation of these alkanes into valuable alkenes. 1,2 Catalytic dehydrogenation of propane and isobutane is performed industrially using noble metal based Pt–Sn or environmentally damaging CrO_x catalysts. Promoter elements such as Sn and Ga are added to Pt in order to improve both the selectivity and stability of the catalyst through both geometric and electronic effects. $^{1,3-5}$ However, these catalysts also deactivate due to sintering and coke formation, necessitating the use of complex catalyst regeneration systems. 1 Catalytic

dehydrogenation of ethane is of particular interest because

Phosphorus (P) is a promising alternative promoter for transition metal-based catalysts. P-Containing catalysts, also known as metal phosphides, are known particularly for hydrodesulfurization, hydrodeoxygenation, and hydrogenation reactions.8-13 Additionally, many metal phosphides are made from earth abundant metals, such as Ni, Co, Mo, and Fe, and have been identified as promising alternatives to noble metal based catalysts for many industrially relevant reactions. 14,15 For light alkane dehydrogenation reactions, P promotion of Ni results in improved selectivity to the desired alkene as well as improved stability over monometallic Ni nanoparticles. 16-19 These enhancements in dehydrogenation performance were attributed to geometric and electronic effects of P incorporation. Specifically, geometric isolation of the metal active sites through the presence of P in the crystal structure helps to limit structure sensitive side reactions, such as hydrogenolysis. 16,17,20,21

ethane constitutes $\sim\!60\%$ of the natural gas liquids in shale gas; however, catalytic ethane dehydrogenation requires higher temperatures than propane or isobutane dehydrogenation, resulting in catalyst instability. 2,6,7 Therefore, novel materials for the catalytic dehydrogenation of ethane are desired that do not rely on noble metals or environmentally toxic materials and have improved stability, particularly at high temperatures, while maintaining desirable ethylene production rates.

^a Department of Chemical and Biomolecular Engineering, University of Notre Dame, Notre Dame, Indiana 46556, USA. E-mail: jhicks3@nd.edu

^b Davidson School of Chemical Engineering, Purdue University, West Lafayette, Indiana 47907, USA

 $[\]dagger$ Electronic supplementary information (ESI) available: Additional experimental details for ICP, pyridine DRIFTS, NH $_3$ TPD, TGA, and 600 °C EDH experiments. TGA results, comparison of Co $_2$ P-E/SBA-15 to literature, variation of H $_2$ composition and ICP results. Full XAS results and fitting parameters, conversion νs . time and additional selectivity data, $k_{\rm d}$ values, pyridine DRIFTS results, NH $_3$ TPD results, thermal background for EDH at 700 °C, Pt-Sn characterization, 24 h TOS EDH data at 700 °C. See DOI: 10.1039/d1cy01737c

Electronic effects from P incorporation lead to a partial positive charge on Ni. This positive charge has been shown to weaken hydrocarbon-metal bonds, resulting selectivity. 16,17,20,21 In our previous work, we synthesized and evaluated Ni₂P for ethane dehydrogenation (EDH) and found that P not only promotes the active metal site but also participates in the reaction pathway. In particular, density functional theory calculations predicted the pathway for deep dehydrogenation of ethylene involves the migration of surface bound ethylene to a Ni-P bridge site, resulting in a higher barrier for deep dehydrogenation of ethylene on Ni2P and suggesting ethylene desorption as the preferred pathway. By preventing deep dehydrogenation, carbon formation during reaction is reduced, which results in improved stability.¹⁶

In this work, we probe the effect of P promotion on Co for EDH. Co was chosen because it is a non-noble metal that has shown promising light alkane dehydrogenation performance when isolated, in oxide form, or promoted with elements such as Zn.22-31 Additionally, Co has geometric site isolation and electronic charge transfer effects upon P incorporation similar to Ni which can benefit dehydrogenation performance.8 We synthesized SBA-15 supported Co-P materials (Co-P/SBA-15) and utilized experimental EDH performance measurements, detailed characterization, and high temperature EDH stability studies to interrogate the effects of varying P content. Increasing P content, resulting in the transition from the Co₂P to the CoP phase, with an optimum in stability found with a P:Co range of 1-2. We further benchmark Co-P/SBA-15 to Pt-Sn, which is highly studied in literature, and showcase the remarkable high temperature stability of the Co-P catalysts over Pt-Sn, demonstrating the tremendous potential of these materials.

2. Experimental

2.1 Materials

Triblock copolymer (P123) was purchased from Aldrich. Hydrochloric acid (37% fuming) was purchased from Merck. Tetraethyl orthosilicate (TEOS, 98%) was purchased from Acros Organics. Cobalt nitrate hexahydrate (Co[NO₃]₂·6H₂O, >98%) and citric acid monohydrate (>99%) were purchased from Alfa Aesar. Ammonium phosphate dibasic ([NH₄]₂HPO₄, 98%) and tin chloride dihydrate (SnCl₂·2H₂O) were purchased from VWR Life Science. Dihydrogen hexachloroplatinate hexahydrate (H₂PtCl₆·6H₂O, >99%) was purchased from BeanTown Chemical. Pyridine was purchased from EDM Millipore. Ethane, hydrogen, helium, 1% oxygen in helium, 2% NH₃ in helium, dry air, and 30% carbon monoxide in helium were purchased from Airgas with a >99% purity. All materials were used as received except pyridine, which was dried over 3 Å molecular sieves and stored in an N₂ dry box before use.

2.2 Synthesis

SBA-15 was used as a support material due to its uniform structure, high surface area, and thermal stability and was

synthesized using literature methods. ³² Approximately 18 g of P123 was dissolved in an aqueous acid solution of 550 g $\rm H_2O$ and 99.5 g HCl. Then, 39.8 g of TEOS was added, followed by holding at 35 °C for 20 hours and then a further heat treatment at 80 °C for 24 hours. The resulting slurry was filtered with ~1000 ml of DI water, dried at 60 °C overnight, and calcined at 550 °C for 6 hours. Before use, the SBA-15 was vacuum dried at <27 Pa for 3 h at 200 °C and stored in an $\rm N_2$ glove box.

Cobalt phosphide catalysts supported on SBA-15 with varying P: Co ratio were synthesized. First Co(NO₃)₂·6H₂O and (NH₄)₂HPO₄ were dissolved in an aqueous citric acid solution to obtain the desired Co weight loading of 5% and P: Co ratio. The Co to citric acid ratio was 1:2. The resulting solution was added to the SBA-15 support using incipient wetness impregnation. The sample was then dried for at least 24 hours at 120 °C followed by calcination at 550 °C for 3 hours. Finally, the material was reduced in approximately 200 ml min⁻¹ H₂ at 700 °C for 2 hours followed by passivation in 1% O2 in He for 1 hour at room temperature. After passivation samples were stored in an N2 dry box until use. The materials with nominal P:Co ratios 0.5, 1, 2, and 4 are denoted Co₂P/SBA-15, Co₂P-E/SBA-15, Co₂P-CoP/SBA-15 and CoP-E/SBA-15 respectively based on the phases from XRD as well as the P:Co ratio from ICP, where E indicates excess P. Cobalt on SBA-15 (Co/SBA-15) was synthesized using the same procedure as the Co-P/SBA-15 materials, simply excluding the $(NH_4)_2HPO_4$.

A platinum tin material supported on SBA-15 was also synthesized (0.5 wt% Pt, 1.5 wt% Sn, denoted Pt–Sn/SBA-15). $H_2PtCl_6\cdot 6H_2O$ and $SnCl_2\cdot 2H_2O$ were dissolved in an aqueous citric acid solution (2:1 citric acid:Pt molar ratio). The resulting solution was added to the SBA-15 support using incipient wetness impregnation. The sample was then dried for at least 24 hours at 120 °C followed by calcination at 550 °C for 3 hours. Finally, the material was reduced in approximately 200 ml min $^{-1}$ H_2 at 550 °C for 2 hours followed by passivation in 1% O_2 in He for 1 hour at room temperature.

2.3 Material characterization

X-ray diffraction was carried out on reduced samples without any further pre-treatment and spent samples after ethane dehydrogenation using a Bruker D8 Advance powder X-ray diffractometer from 20–60 2θ .

 N_2 physisorption was conducted using a Quantachrome NOVA 2200e on reduced samples without any further pretreatment. The surface area was calculated using the multipoint Brunauer–Emmett–Teller (BET) method from 0.05–0.3 P/P_0 . Pore size and pore volume of porous samples were calculated using the Barrett–Joyner–Halenda (BJH) method applied to the adsorption isotherm.

Samples for CO pulse chemisorption were first pre-treated at 550 $^{\circ}$ C under flowing H₂ for 2 h. CO pulse was performed at 35 $^{\circ}$ C with injections of 30% CO in He. Injections were

continued until saturation occurred. Temperature programmed oxidation (TPO) was performed on select catalysts after ethane dehydrogenation using an Autosorb IQ equipped with a mass spectrometer. The sample was pretreated in He at 200 °C for 2 h. The sample was then cooled to room temperature and then heated from 40 °C to 1000 °C at 10 °C min⁻¹ in a stream of 1% O₂ in He. The total carbon deposited on the catalyst was calculated using m/z =44 for CO_2 and m/z = 28 corrected for the contribution from CO₂ for CO.

Transmission electron microscopy (TEM) was performed on reduced and passivated samples without any further pretreatment using a JEOL 2011 set to 120 or 200 kV. The powder sample was suspended in acetone using sonication and then drop cast onto a carbon coated copper grid. The grid was then dried overnight in a desiccator before analysis.

In situ X-ray absorption spectroscopy (XAS) experiments were performed at the 10-BM beamline at the advanced photon source (APS) at Argonne National Laboratory. Measurements were performed at the Co K (7.709 keV) edge. Samples were pressed into a stainless-steel sample holder and placed in a quartz tube sample cell. The materials were evaluated post calcination (i.e. no 700 °C reduction) and after reduction. For the post calcination materials, the cell was sealed and purged with He at room temperature prior to measurement. For reduced samples the cell was sealed and treated at 550 °C in 3.5% H2 to remove surface oxides from air exposure following synthesis. The cell was cooled to room temperature in He, and then transferred to the beamline. All measurements were performed in transmission mode in fast scan from 250 eV below the edge to 800 eV above the edge, which took approximately 10 minutes per scan. The data were interpreted using WinXAS 3.1 software to find the coordination number (CN) and bond distance (R) using standard procedures.

Feff6 was used to develop a model to fit these samples at the Co K edge using crystallographic information files (CIF) for CoO and Co2P. Based on the geometric arrangement of atoms in the CIF found on the materials project database, theoretical phase and amplitude files were also created for Co-Co (CN = 12, R = 2.51 Å), Co-P (CN = 1, R = 2.31 Å), Co-O (CN = 1, R = 2.13 Å), and Co-Co (CN = 1, R = 2.60 Å) scattering pairs. 33,34 The S₀2 was calibrated by fitting the metal foil and was found to be 0.71. A least squared fit the first shell of r-space was performed on the k^2 weighted Fourier transform data over the range 2.7 to 11.0 Å⁻¹ to fit the magnitude and imaginary components. The standard errors in the fits are CN \pm 10%, BD \pm 0.03 Å, and sigma² \pm 0.001.

CO adsorption diffuse reflectance infrared Fourier transform spectroscopy (DRIFTS) experiments used approximately 80 mg of KBr placed into the sample cup followed by approximately 20 mg of the Co-P/SBA-15 sample which was pressed flat on top. The sample was pre-treated in situ with 30 ml min⁻¹ of H₂ for 2 hours at 315 °C (temperature limit of the DRIFTS cell). The cell was then purged for 30 min with 100 ml min⁻¹ He and 30 ml min⁻¹ N₂. Next the cell was cooled to 30 °C. After the temperature stabilized, background spectra were taken. Next, a stream of 30% CO in He was passed over the sample for 1 hour. Then the cell was purged with the same gas flows used for purging as above until the spectra stabilized. Spectra were taken using a Bruker Vertex FTIR spectrometer equipped with a mercury cadmium tellurium detector. The spectra were an average of 200 scans taken from 4000 cm⁻¹ to 400 cm⁻¹ at a 2 cm⁻¹ resolution.

2.4 Ethane dehydrogenation

Ethane dehydrogenation experiments were conducted in a custom-built reactor system with a 5 mm ID quartz reactor. The reactor effluent was analysed using an inline SRI Model #5 gas chromatograph equipped with an alumina column (Restek Cat #79728) and TCD and FID detectors. Before reaction, samples were pre-treated at 550 °C under 30 ml min⁻¹ H₂ for 1 h, the reactor was then heated to the desired reaction temperature at 10 °C min⁻¹ and allowed to stabilize prior to switching to the reaction feed composition. Catalytic results from Co-P/SBA-15 materials were compared at 600 °C and 700 °C with a feed of 5% ethane and 5% hydrogen (unless otherwise specified) in a balance of He with a total flow of 100 ml min⁻¹. At 600 °C, the catalyst mass was varied from 1-40 mg (Table S1†) to obtain similar initial conversions in the range of 0.6-2%. At 700 °C, 5 mg of catalyst was used for all experiments. The carbon balance for all experiments was >98%. Gas phase carbon selectivity was determined using eqn (1), where C_i is the concentration of product i and n_i is the carbon number of product i. Ethylene site time yield (STY) was calculated using eqn (2). Rates were extrapolated to t = 0 to obtain initial rates by fitting the data to eqn (3) where t is the time and the rate at t = 0 is $r_i + r_{\rm f}$.

Ethylene Carbon Selectivity =
$$\frac{2 \times C_{C_2H_6}}{\sum C_i n_i}$$
 (1)

$$\label{eq:ethylene} \text{Ethylene Site Time Yield} \left(\text{STY} \right) = \frac{\mu \text{mol ethylene}}{\text{min} \cdot \mu \text{mol CO site}} \tag{2}$$

$$r(t) = r_i^{-\alpha t} + r_f \tag{3}$$

Catalyst stability was analysed by fitting the conversion as a function of time to eqn (4) which is based on a linear deactivation model. $X_{\rm E}$ is the ethane conversion at time t, $X_{\rm EO}$ is the initial conversion, and $k_{\rm d}$ is the deactivation constant.

$$\ln\left(\frac{1-X_{\rm E}}{X_{\rm E}}\right) = k_{\rm d}t + \ln\left(\frac{1-X_{\rm E0}}{X_{\rm E0}}\right) \tag{4}$$

3. Results and discussion

We begin by comparing the EDH performance of Co/SBA-15 to Co₂P-E/SBA-15 (nominal P:Co of 1 with 5 wt% Co) at 600

Table 1 EDH performance of Co/SBA-15 and Co₂P-E/SBA-15. Reaction conditions were 600 $^{\circ}$ C, 5% C₂H₆, 5% H₂

Material	Initial ethylene selectivity (%)	Initial ethylene STY ^a (min ⁻¹)	$k_{\rm d}~({ m h}^{-1})$	
Co ₂ P-E/SBA-15	88	22	0.16	
Co/SBA-15	41	0.8	0.31	

^a μmol ethylene/min μmol CO sites.

°C (Table 1). The EDH reactions were conducted using a packed bed reactor with a feed stream containing 5% ethane and 5% H₂ (He balance). As shown in Table 1, Co₂P-E/SBA-15 drastically outperforms Co/SBA-15 in terms of ethylene selectivity as well as ethylene production. Additionally, the deactivation rate constant (k_d) , which is determined from the first order deactivation model shown in eqn (4), is approximately 2 times smaller for Co₂P-E/SBA-15 relative to Co/SBA-15, indicating a more stable catalyst. Carbon formation on the catalysts after EDH was measured using TGA (Fig. S1†). Both Co/SBA-15 and Co₂P-E/SBA-15 showed less than 1% mass loss between 250-800 °C, indicating very little carbon deposition during EDH under these reaction conditions. These results demonstrate that P incorporation significantly enhances the EDH performance of Co, which is consistent with the trends observed for light alkane dehydrogenation with other P promoted metals such as Ni, Ru, and Pt. 16-20,36 Co₂P-E/SBA-15 was compared to reported catalytic results of EDH in literature and displayed comparable TOF values to Pt based alloys and other materials tested for EDH (Table S2†). The H₂ to C₂H₆ ratio for Co₂P-E/ SBA-15 was also varied from 0:1 to 1:1 (Fig. S2†). The ethylene STY as well as the stability increased with increasing H₂ content in the feed. This is similar to what was observed by Galvita et al. who reported different H2 concentrations with Pt/Mg(Al)O for EDH.³⁷ The ethylene selectivity decreases slightly with increasing H2 content, varying from approximately 88-97%. This is a similar trend to the results observed for Pt/Mg(Al)O; however the selectivity decrease is far less pronounced for Co₂P-E/SBA-15.³⁷

To further probe the effect of P on EDH performance, we varied the P:Co molar ratio from 0 to 4. The XRD patterns are shown in Fig. 1. All samples show a very broad feature around 20–30° 2θ from the amorphous silica of the SBA-15 support. The samples with P:Co ratios of 0.5 and 1 show a peak at approximately $40^{\circ} 2\theta$ corresponding to the (211) and (021) planes and another peak at 43° 2θ corresponding to the (121) and (310) planes of the Co₂P phase. As the P:Co ratio is further increased, new features appear at 48°, 36°, and 31- $32^{\circ} \ 2\theta$ consistent with the (121) and (220), (111) and (210), and (101) and (200) planes of the CoP phase, respectively. This results in a mixture of orthorhombic Co₂P and orthorhombic CoP phases in the P:Co ratio of 2 material and a XRD pure CoP phase with a P:Co ratio of 4. The P:Co ratio and Co weight loading from ICP analysis are provided in Table S3.† The actual P: Co ratio is lower than the nominal

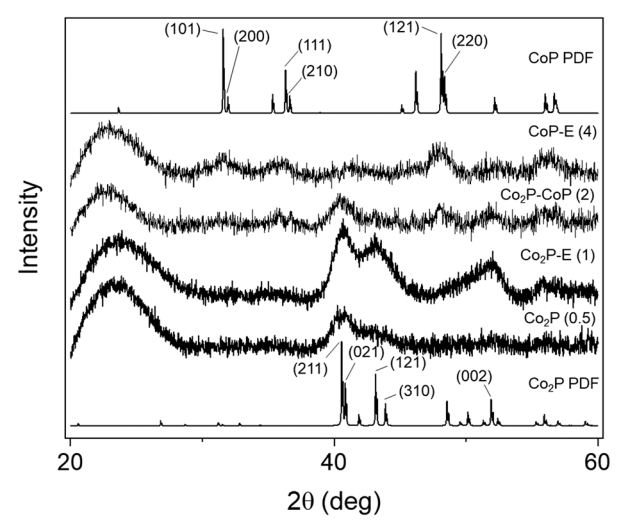


Fig. 1 XRD of Co-P samples with varying P:Co ratios shown in parentheses.

value due to P loss during the reduction step, particularly for the higher P content materials.⁸

The crystallite sizes for the synthesized catalysts were calculated with the Scherrer equation and were within the 2-6 nm range for all materials (Table 2). Particle size from TEM of select materials (Table 2) showed little variation between samples, in line with the crystallite size observed in XRD. The surface area, pore size, and pore volume are also provided in Table 2. The surface area decreases for the highest P content samples, consistent with higher loadings of material on SBA-15.38 A decrease in CO uptake and Co dispersion are also observed with CoP-E/SBA-15, potentially due to excess P species blocking Co sites. This is similar to what is reported by Burns et al., where the highest P content Co-P material had the lowest surface area and O₂ uptake.⁸ The surface area, pore size, pore volume, and particle size of Co/SBA-15 and Co₂P-E/SBA-15 are similar, indicating the difference in EHD performance between Co/SBA-15 and Co₂P-E/SBA-15 (Table 1) is not due to differences in the textural properties.

XAS was used to analyse both the oxidation state (XANES) and local structure (EXAFS) of Co/SBA-15 and Co₂P-E/SBA-15 (Table S4 and Fig. S3†). We measured both the post calcination and reduced samples. Both Co/SBA-15 and Co₂P-E/SBA-15 show a reduction in XANES energy and lower white line intensity from the oxide precursors (calcined) to the H₂ treated (reduced) sample consistent with a loss of Co²⁺ to Co⁰ atoms. Analysis of the EXAFS region shows that before reduction both Co/SBA-15 and Co₂P-E/SBA-15 contain Co-O bonds of ~2.0 Å. This is consistent with bond distances reported in literature for cobalt oxides. 26,28,39 Upon reduction Co-Co (2.5 Å) bonds form in the Co/SBA-15 sample. When reduced, Co₂P-E/SBA-15 formed both Co-Co (2.6 Å) and Co-P (2.37 Å) bonds. This is similar to Co-P bond distances reported in literature for Co-P materials (~2.3 Å). 13,40,41 Some residual Co-O bonds were also observed in the Co₂P-E/

Material	P:CO ratio	BET surface area (m² g ⁻¹)	Average pore size (nm)	Average pore volume (cm ³ g ⁻¹)	Crystallite size ^a (nm)	Particle size ^b (nm)	CO uptake (μmol g ⁻¹)	Co disp
SBA-15	_	810	6.8	0.61	_	_	_	_
Co/SBA-15	Λ	440	6.7	0.42	2	5.1 + 1.2	0	1.0

Material	ratio	area (m ² g ⁻¹)	Average pore size (nm)	volume (cm ³ g ⁻¹)	size ^a (nm)	size ^b (nm)	CO uptake (μmol g ⁻¹)	(%)
SBA-15	_	810	6.8	0.61	_	_	_	_
Co/SBA-15	0	440	6.7	0.42	2	5.1 ± 1.2	9	1.0
Co ₂ P/SBA-15	0.5	320	6.0	0.43	5	_	56	6.9
Co ₂ P-E/SBA-15	1	400	5.9	0.40	4	6.2 ± 2.5	63	7.0
Co ₂ P-CoP/SBA-15	2	250	5.9	0.31	6	_	58	6.6
CoP-E/SBA-15	4	220	5.9	0.31	5	4.0 ± 1.2	26	3.9

^a From Scherrer equation. ^b From TEM. ^c [CO uptake (μmol g⁻¹)/Co from ICP (μmol g⁻¹)] × 100.

SBA-15 material after reduction, likely due to interaction of the nanoparticles with the support. However, the material is not in a bulk oxide state, as shown by the XANES energy and lack of a second shell Co-O-Co feature in EXAFS (Fig. S3.d†). Reduced Co/SBA-15 (5.3) had more Co-Co bonds than reduced Co₂P/SBA-15 (1.0), indicating smaller Co ensembles in Co₂P-E/SBA-15. A longer Co-Co bond distance was also observed in Co/SBA-15 (2.5 Å) than Co₂P-E/SBA-15 (2.6 Å), consistent with literature Co₂P structures.⁴⁰ These results indicate that Co atoms are more isolated in the Co₂P-E/SBA-15 material, which is what would be expected with the addition of P atoms to form the Co₂P phase. For alkane dehydrogenation reactions, enhanced active site isolation has been shown to minimize hydrogenolysis pathways by limiting the size of metal ensembles. 1,5,7 The increased site isolation improved selectivity and stability results in dehydrogenation and is a likely cause for the improved ethylene production rates, ethylene selectivity, and stability of Co₂P-E/SBA-15 relative to Co/SBA-15.

Table 2 Physisorption results, crystallite size, and CO uptake

We performed EDH activity tests of the various P:Co ratio materials at 600 °C. Conversions were <2% to remain in the kinetically limited regime (Fig. S4†) and to avoid effects from equilibrium (equilibrium conversion at these conditions is 32%). The only gas phase products observed were ethylene and methane. Initial gas phase ethylene selectivity as a function of P:Co ratio is shown in Fig. 2a. Co/SBA-15 has a poor ethylene selectivity of 41%. Upon increasing the P:Co ratio to 0.5 the ethylene selectivity significantly increases to 85%. This highlights the significant contribution that a small amount of P can have on the ethylene selectivity. Upon further increase of the P:Co ratio between 1 to 4 the ethylene selectivity further increases slightly to approximately 88%. This indicates that for materials with a P:Co ratio in this range, the geometric and electronic properties, which are the likely cause of the selectivity improvement, have been modified to the point that the gas phase ethylene selectivity at these conditions is no longer a strong function of P content. Initial and steady state ethylene and methane selectivities for all catalysts are shown in Table S5.† All materials showed increased ethylene selectivity at longer TOS. The ethylene selectivity of Co/SBA-15 remained well below the ethylene selectivity of the Co-P/SBA-15 materials.

Fig. 2a also shows the site normalized ethylene production rates (obtained from CO chemisorption) as a function of time for the different P:Co ratio materials. Co/SBA-15 shows very low ethylene production, with the primary gas phase product being methane. All of the Co-P/SBA-15 materials show increased ethylene STY over Co/SBA-15. Co₂P/SBA-15 has the highest initial ethylene STY. Upon further increase of the P: Co ratio there is a decrease in ethylene STY for Co₂P-E/SBA-

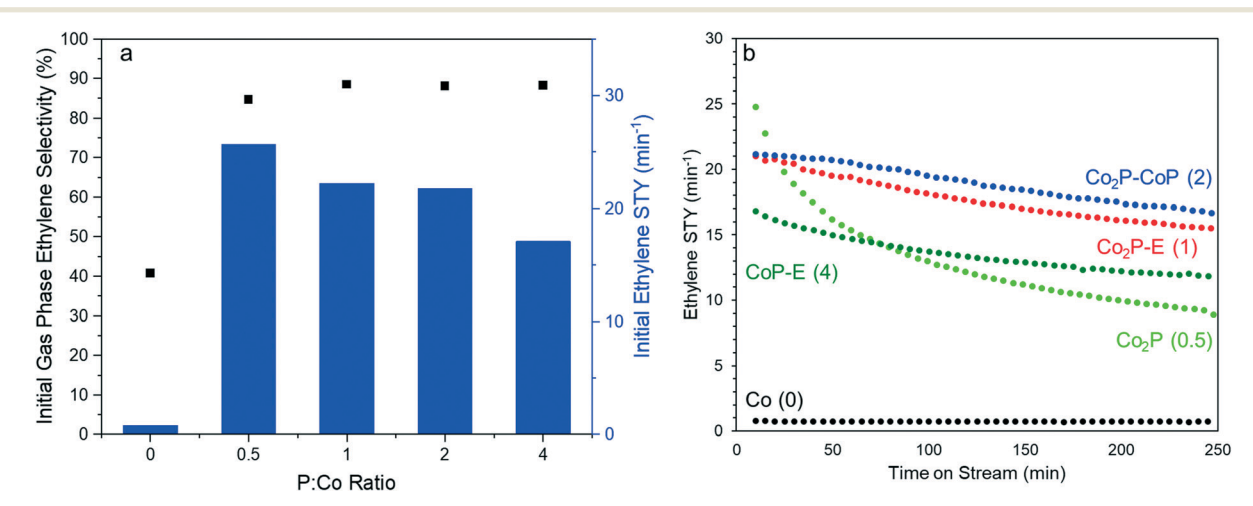


Fig. 2 a) Initial gas phase ethylene selectivity and initial ethylene STY. b) Ethylene STY for different P: Co ratios as a function of time. The values in parentheses are the nominal P: Co ratio. Reaction conditions were 600 °C, 5% C₂H₆, 5% H₂, balance He, 100 ml min⁻¹ total flow.

15 and Co₂P-CoP/SBA-15, which have similar ethylene STY, followed by a further decrease for CoP-E/SBA-15. This is similar to the trend observed by Lan et al. for furfural hydrodeoxygenation when varying the P: Co ratio. 42

While Co₂P/SBA-15 has the highest initial ethylene STY, it also has the highest rate of deactivation. This can be seen from the loss in the ethylene STY with time shown in Fig. 2b. The Co₂P-E/SBA-15 and Co₂P-CoP/SBA-15 materials, which have a higher P content, both show more stable ethylene STY than Co₂P/SBA-15. Upon further increase of the P content (CoP-E/SBA-15) the ethylene STY stability decreased compared to Co₂P-E/SBA-15 and Co₂P-CoP/SBA-15. A similar trend is observed in the calculated k_d values (Fig. S5†), where the P:Co 1 and 2 materials show the lowest values, indicating the highest stability. This indicates some P has a beneficial impact on stability, but significant amounts of excess P can promote deactivation.

The electronic state of the surface Co sites were probed using CO adsorption DRIFTS analysis. After pre-treatment the samples were cooled to room temperature, saturated with CO and then purged to remove gas phase species. The results are shown in Fig. 3. In the Co/SBA-15 sample, features at 2002 cm⁻¹ and 2024 cm⁻¹ are present. These features are consistent with CO linearly bound to Co⁰, which is reported between 2080–1990 cm⁻¹. The existence of two features in the linearly bonded CO region indicates the existence of multiple adsorption sites with the lower wavenumber feature corresponding to a lower coordination site. 43 Bridge bonded CO on Co, which has been reported in the range 1950-1820 cm⁻¹, was not observed.^{8,44-47} This is consistent with other reports of supported Co catalysts at similar weight loadings to this study. 48,49 The Co-P/SBA-15 samples have a feature at approximately 2060 cm⁻¹, which is not observed with Co/SBA-15. Features in this region have been

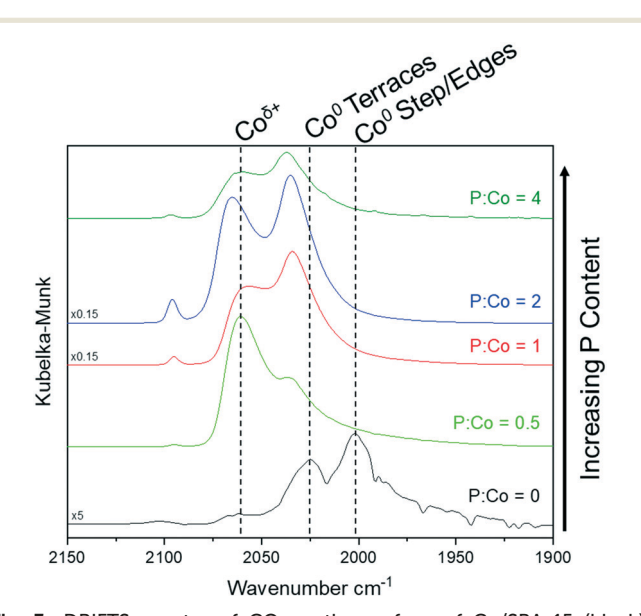


Fig. 3 DRIFTS spectra of CO on the surface of Co/SBA-15 (black), Co₂P/SBA-15 (light green), Co₂P-E/SBA-15 (red) Co₂P-CoP/SBA-15 (blue) and CoP-E/SBA-15 (dark green).

assigned in literature to $Co^{\delta+}$ sites. 44,48,50 Additionally, this shift to higher wavenumbers for room temperature CO adsorption IR studies has been seen in other metal phosphides which have partially positively charged metal sites. 12,20,51 There were no noticeable trends in the 2060 cm⁻¹ peak with P content. This is not surprising due to the complex nature of the catalyst surface with varying P: Co ratio as both the phase as well as the amount of excess P on the surface varies (Fig. 4). The wavenumber of the 2060 cm⁻¹ feature only varies slightly (±5 cm⁻¹) between the different P:Co ratio materials. The similarity of the electronic properties shown by CO FTIR, as well as the minor differences in ethylene STY as a function of P: CO ratio, indicates the active sites in these materials ($Co^{\delta+}$ sites) behave similarly with P incorporation. These partially positively charged metal active sites in metal phosphides have been shown to weaken hydrocarbon bonds with the metal. 16,20,52,53 These weaker bonds result in lower barriers for hydrocarbon desorption, leading to improved selectivity and stability dehydrogenation. The electronic modifications to Pt caused by Sn and Zn have been shown to result in a similar weakening of metal to hydrocarbon bonds. 3,54,55 The reduced hydrocarbon bonding on the $\operatorname{Co}^{\delta^+}$ sites is a potential reason for the improvement in EDH performance for the Co-P/SBA-15 materials relative to Co/SBA-15.

Fig. 4 depicts a hypothesized representation of the surface of the Co-P/SBA-15 materials based on the results from XRD, CO DRIFTS, and the presence of excess P based on the P:Co ratio and stoichiometry of phases present. The images for Co₂P/SBA-15 and Co₂P-E/SBA-15 utilize a side view of the (211) plane, the Co₂P-CoP/SBA-15 and CoP-E/SBA-15 depict a side view of the (121) plane, and Co/SBA-15 depicts a side view of the (111) plane. Here we see that Co/SBA-15 has reduced cobalt sites, leading to low selectivity to ethylene. $Co_2P/SBA-15$ has $Co^{\delta+}$ sites and increased separation of Coatoms relative to Co/SBA-15, possibly resulting in the observed improvement in selectivity. The selectivity further improves in the Co₂P-E/SBA-15 material where the P species on the surface are likely aiding in blocking overactive, lower coordination sites, allowing for a further increase in ethylene selectivity as well as stability. Co₂P-CoP/SBA-15 contains the CoP phase which has a higher degree of Co atom separation as well as surface P species, resulting in similar ethylene selectivity to Co₂P-E/SBA-15 and slightly better stability. CoP-E/SBA-15 has similar $Co^{\delta+}$ sites as the other Co-P/SBA-15 materials, resulting in high selectivity; however, there is a slight decrease in stability. A similar trend was reported by Cecilia et al. where an optimum in stability for hydrodechlorination using Co-P materials was observed in

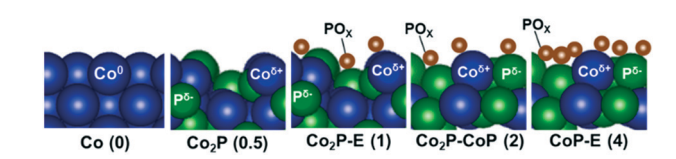


Fig. 4 Phase (P:Co ratio) and proposed surface for the different Co-P/SBA-15 materials

the P:Co ratio range of 1.5-2.56 In results reported for Ni₂P by Zhu et al., an optimum in isobutene dehydrogenation performance was observed with a P:Ni ratio of 1.17 The authors concluded that the negative impact of excess P on isobutane dehydrogenation performance was due to the acidity of PO_r species promoting unwanted side reactions. The excess P present in the CoP-E/SBA-15 material in this work may be acting in a similar manner. Thus, we evaluated the acidity using pyridine DRIFTS experiments (Fig. S6†) of Co/SBA-15 and CoP-E/SBA-15. There was not a significant difference in the type of sites present in Co/SBA-15 and CoP-E/SBA-15, with both materials displaying features associated with Lewis acidity and not Brønsted acidity. 11,12 Previous reports of pyridine IR experiments with metal phosphides suggest that the features associated with Brønsted acidity are often very small or non-existent. 11,12,17,57 These results, showing little to no Brønsted acidity, are consistent with the high selectivity (≥88%) observed with the CoP-E/SBA-15 material because Brønsted acid sites would likely lead to lower olefin selectivity. 1,58 The acidity was further analysed using NH3 TPD. The relative amount of acid sites to metal sites increases when increasing the P:Co ratio (Fig. S7†). This trend indicates that the excess P species on the surface have acidic character and may participate in surface reactions.

Co₂P-E/SBA-15 was one of the most stable materials at 600 °C and had one of the highest ethylene STY; therefore, this material was chosen for further evaluation at 700 °C (Fig. 5). Co₂P-E/SBA-15 maintained extremely stable ethylene production, showing no decrease in ethylene production over 4 h TOS and remaining above the thermal background reactivity (Fig. S8†) which is present at these high temperatures.⁵⁹ The conversion also remained stable with time on stream (Fig. S9†). Co₂P-E/SBA-15 also showed high

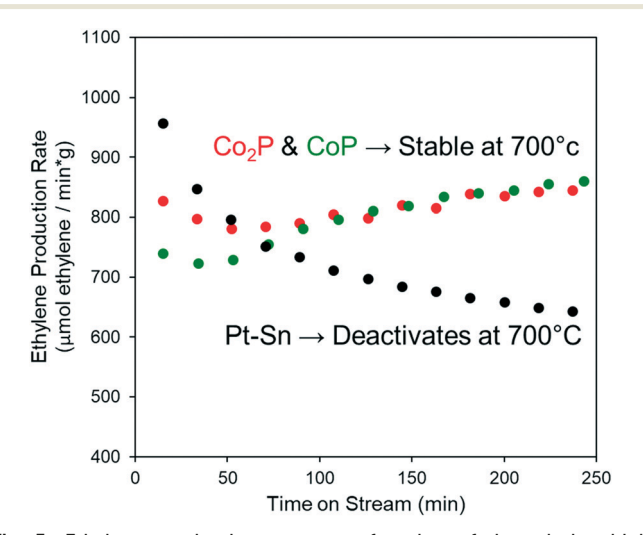


Fig. 5 Ethylene production rate as a function of time during high temperature EDH for Co₂P-E/SBA-15 (red), CoP-E/SBA-15 (green) and Pt-Sn/SBA-15 (black). Reaction conditions were 700 °C, 5% C₂H₆, 5% H_2 .

gas phase ethylene selectivity of 98%. Ethylene and methane selectivity for Co-P materials tested at these conditions were similar to each other and remained fairly stable over time. (Table S6†). Additionally, we evaluated a Pt-Sn/SBA-15 material at these higher temperatures in order to benchmark to a known catalyst. Physisorption, particle size, and CO uptake results for Pt-Sn/SBA-15 are given in Table S7.† Pt-Sn/ SBA-15 started out with higher ethylene production rates than Co₂P-E/SBA-15 but deactivated to a similar ethylene production rate to that of Co₂P-E/SBA-15 after approximately 70 min TOS and then continued to decrease. These results are consistent with literature for Pt-based materials, particularly at high temperatures. 59-61 Although Pt alloys are known to be highly active and stable dehydrogenation catalysts at lower temperatures, at higher temperatures Pt alloys show significant deactivation.⁵⁹

To further investigate the stability of Co₂P-E/SBA-15, analysis of the spent catalyst after 4 h TOS was conducted. Carbon formation is a common cause of deactivation for dehydrogenation catalysts and was investigated using temperature programmed oxidation (TPO) experiments.^{1,7} After EDH at 700 °C, Co₂P-E/SBA-15, CoP-E/SBA-15, and Pt-Sn/SBA-15 had 52, 24, and 15 mg C per g catalyst, respectively. Literature has shown that carbon deposition does not necessarily correlate with poor catalyst stability if the formed carbon does not block active sites that lead to the

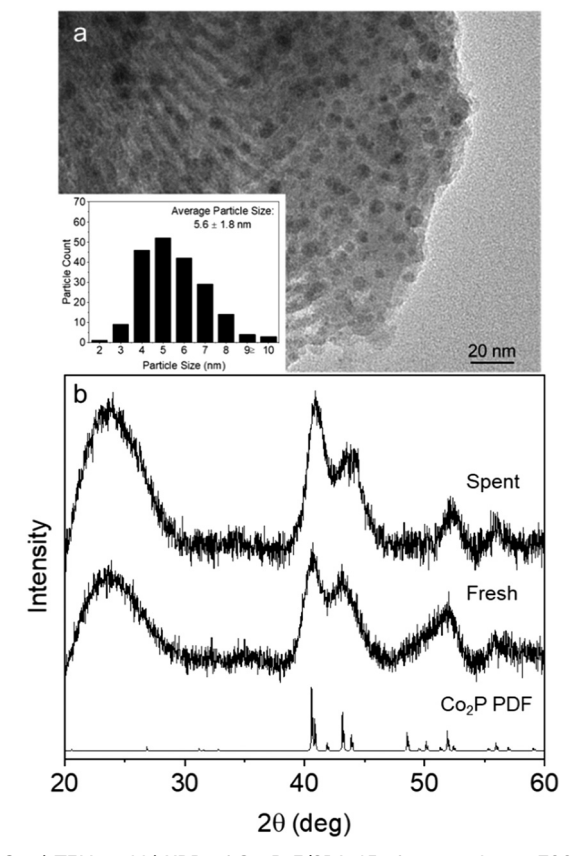


Fig. 6 a) TEM and b) XRD of Co₂P-E/SBA-15 after reaction at 700 °C.

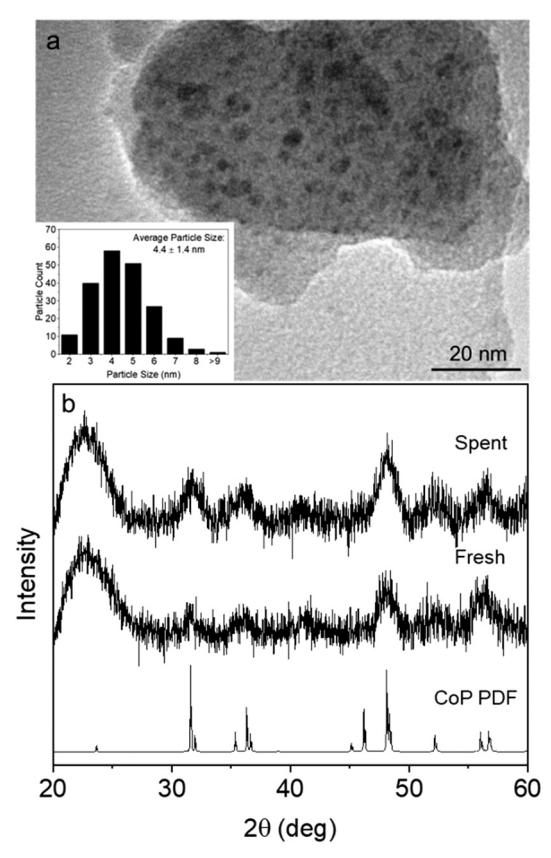


Fig. 7 a) TEM and b) XRD of CoP-E/SBA-15 after reaction at 700 °C.

desired product. 62,63 Based on the stability in the ethylene production rate with time, we can conclude this is likely the case for Co-P/SBA-15 materials, where the carbon formed is not negatively affecting the ethylene production sites. TEM of Co₂P-E/SBA-15 post-reaction is shown in Fig. 6a. The average particle size of Co₂P-E/SBA-15 before (6.2 nm) and after reaction (5.6 nm) is nearly the same. The particle size distribution is also similar before and after reaction (5 nm before and after reaction). This shows that there is little to no sintering of Co₂P-E/SBA-15 during reaction at 700 °C. This is corroborated by the crystallite size analysis from XRD for Co₂P-E/SBA-15, which remains virtually invariant before (4 nm) and after reaction (5 nm). XRD of post reaction Co₂P-E/ SBA-15 (Fig. 6b) also shows that the Co₂P phase remains intact during reaction. This highlights the high thermal stability of Co₂P-E/SBA-15. This is in contrast to Pt-Sn/SBA-15. Before reaction, the XRD contains a complex mixture of Pt-Sn phases (Fig. S10†). After reaction, Pt-Sn/SBA-15 shows a decrease in the intensity of the peaks associated with the PtSn₂ phase relative to the Pt₃Sn and PtSn phases. This shift in phase during reaction is a possible cause of the deactivation of Pt-Sn/SBA-15.64

To understand if this high temperature stability was affected by varying P content, we also tested CoP-E/SBA-15 at 700 °C (Fig. 5). CoP-E/SBA-15 shows similar, extremely stable, ethylene production rates as well as high ethylene selectivity (98%) at 700 °C. Furthermore, the particle size from TEM

(Fig. 7a) and crystallite size from XRD (5 nm both before and after reaction) showed no signs of sintering during reaction at 700 °C. The CoP phase of the material also remains intact after reaction (Fig. 7b), demonstrating the remarkable stability of the Co₂P–E/SBA-15 material applies to other Co–P/SBA-15 materials as well.

EDH data collected for 24 h TOS is provided in Fig. S11.† As expected, Pt–Sn/SBA-15 continues to deactivate with time. However, both Co–P/SBA-15 materials show some small initial deactivation followed by increased ethylene production with time until they start to plateau toward the end of the 24 h period. This increase in ethylene production rate corresponds to an increase in conversion from approximately 2% to 3%. This type of behaviour, particularly at high temperatures, during EDH has been previously reported for VO_x , In, and Pt–In materials. $^{65-67}$ This increase may be due to the formation of active carbon species on the catalyst with time, as well as surface rearrangements that expose additional sites or create new active sites. 65,67 These results help to highlight the remarkable high temperature EDH stability of the Co–P/SBA-15 materials.

4. Conclusions

Herein, we have shown that Co-P/SBA-15 materials are active, selective and stable for EDH. Co-P/SBA-15 materials displayed improved dehydrogenation performance over Co/ SBA-15. This is most likely due to both geometric site isolation of Co sites and charge transfer between the Co atoms and P in the Co-P/SBA-15 materials. Ethylene production rates and stability are maximized in the P:Co ratio 1-2 range due to an optimum in the ensemble size of Co atoms while minimizing excess P. Both Co₂P-E/SBA-15 and CoP-E/SBA-15 show remarkable high temperature stability, showing little to no deactivation in ethylene production over 4 h while maintaining an ethylene selectivity of >98%. Both Co-P/SBA-15 materials also showed enhanced stability at 700 °C compared to Pt-Sn/SBA-15. The Co-P/SBA-15 materials maintained the same phases observed before reaction and showed no signs of sintering. Overall, these results provide strong support for the use of Co-P materials for high temperature dehydrogenation reactions, which may be further improved with other non-noble metal phosphides or bimetallic phosphide compositions.

Conflicts of interest

There are no conflicts to declare.

Acknowledgements

This work was supported primarily by the Engineering Research Centers Program of the National Science Foundation under NSF Cooperative Agreement no. EEC-1647722. The authors would like to thank the Defence University Research Instrumentation Program under AFOSR Award no. FA9550-17-1-0376. The authors would also like to

thank the Notre Dame Integrated Imaging Facility, the Notre Dame Molecular Structure Facility, and Notre Dame Centre for Environmental Science and Technology for use of their facilities.

Notes and references

- 1 J. J. H. B. Sattler, J. Ruiz-Martinez, E. Santillan-Jimenez and B. M. Weckhuysen, Chem. Rev., 2014, 114, 10613-10653.
- 2 T. Ridha, Y. Li, E. Gençer, J. Siirola, J. Miller, F. Ribeiro and R. Agrawal, *Processes*, 2018, 6, 139.
- 3 V. J. Cybulskis, B. C. Bukowski, H. T. Tseng, J. R. Gallagher, Z. Wu, E. Wegener, A. J. Kropf, B. Ravel, F. H. Ribeiro, J. Greeley and J. T. Miller, ACS Catal., 2017, 7, 4173-4181.
- 4 D. E. Resasco, *Encyclopedia of Catalysis*, 2003, vol. 3, pp. 49–79.
- 5 Y. Dai, X. Gao, Q. Wang, X. Wan, C. Zhou and Y. Yang, Chem. Soc. Rev., 2021, 50, 5590-5630.
- 6 R. C. Burruss and R. T. Ryder, Open-File Rep. U. S. Geol. Surv., 2014, 38.
- 7 H. Saito and Y. Sekine, RSC Adv., 2020, 10, 21427–21453.
- 8 A. W. Burns, K. A. Layman, D. H. Bale and M. E. Bussell, Appl. Catal., A, 2008, 343, 68-76.
- 9 Y. Bonita, T. P. O'Connell, H. E. Miller and J. C. Hicks, Ind. Eng. Chem. Res., 2019, 58, 3650-3658.
- 10 Y. Bonita and J. C. Hicks, J. Phys. Chem. C, 2018, 122, 13322-13332
- 11 Y. Bonita, V. Jain, F. Geng, T. P. O'Connell, N. X. Ramos, N. Rai and J. C. Hicks, Appl. Catal., B, 2020, 277, 119272.
- 12 Y. K. Lee and S. T. Oyama, J. Catal., 2006, 239, 376-389.
- 13 M. F. Delley, Z. Wu, M. E. Mundy, D. Ung, B. M. Cossairt, H. Wang and J. M. Mayer, J. Am. Chem. Soc., 2019, 141, 15390-15402.
- 14 P. Liu, Y.-L. Zhu, L. Zhou, W.-H. Zhang and Y.-X. Li, Catal. Lett., 2020, 150, 2695-2702.
- 15 G. Yun, Q. Guan and W. Li, RSC Adv., 2017, 7, 8677-8687.
- 16 J. Ko, J. A. Muhlenkamp, Y. Bonita, N. J. LiBretto, J. T. Miller, J. C. Hicks and W. F. Schneider, Ind. Eng. Chem. Res., 2020, 59, 12666-12676.
- 17 Q. Zhu, H. Zhang, S. Zhang, G. Wang, X. Zhu and C. Li, Ind. Eng. Chem. Res., 2019, 58, 7834-7843.
- 18 Y. Xu, H. Sang, K. Wang and X. Wang, Appl. Surf. Sci., 2014, 316, 163-170.
- 19 Y. Yao, M. Zuo, H. Zhou, J. Li, H. Shao, T. Jiang, X. Liao and S. Lu, ChemistrySelect, 2018, 3, 10532-10536.
- 20 R. Ma, T. Yang, J. Gao, J. Kou, J. Z. Chen, Y. He, J. T. Miller and D. Li, ACS Catal., 2020, 10, 10243-10252.
- 21 S. A. Chang and D. W. Flaherty, J. Phys. Chem. C, 2016, 120, 25425-25435.
- 22 H. Guo, C. Miao, W. Hua, Y. Yue and Z. Gao, Microporous Mesoporous Mater., 2021, 312, 110791.
- 23 R. Huang, Y. Cheng, Y. Ji and R. J. Gorte, Nanomaterials, 2020, 10, 244.
- 24 Y. Zhao, H. Sohn, B. Hu, J. Niklas, O. G. Poluektov, J. Tian, M. Delferro and A. S. Hock, ACS Omega, 2018, 3, 11117–11127.
- 25 W. Li, S. Y. Yu, G. D. Meitzner and E. Iglesia, J. Phys. Chem. B, 2001, 105, 1176-1184.

- 26 B. Hu, W. G. Kim, T. P. Sulmonetti, M. L. Sarazen, S. Tan, J. So, Y. Liu, R. S. Dixit, S. Nair and C. W. Jones, ChemCatChem, 2017, 9, 3330-3337.
- 27 L. G. Cesar, C. Yang, Z. Lu, Y. Ren, G. Zhang and J. T. Miller, ACS Catal., 2019, 9, 5231-5244.
- 28 L. Wu, Z. Ren, Y. He, M. Yang, Y. Yu, Y. Liu, L. Tan and Tang, ACS Appl. Mater. Interfaces, 48934-48948.
- 29 K. Wakui, K. Satoh, G. Sawada, K. Shiozawa, K. Matano, K. Suzuki, T. Hayakawa, Y. Yoshimura, K. Murata and F. Mizukami, Catal. Lett., 2002, 81, 83-88.
- 30 Z. Bian, N. Dewangan, Z. Wang, S. Pati, S. Xi, A. Borgna, H. Kus and S. Kawi, ACS Appl. Nano Mater., 2021, 4, 1112-1125.
- 31 Y. Gao, L. Peng, J. Long, Y. Wu, Y. Dai and Y. Yang, Microporous Mesoporous Mater., 2021, 323, 111187.
- 32 D. Zhao, J. Feng, Q. Huo, N. Melosh, G. H. Fredrickson, B. F. Chmelka and G. D. Stucky, Science, 1998, 279, 548-552.
- Materials Data on CoO (SG:225) by 33 K. Persson, Materials Project, https://materialsproject.org/materials/mp-
- 34 K. Persson, Materials Data on Co2P (SG:62) by Materials
- 35 C. Costa, J. M. Lopes, F. Lemos and F. Ramôa Ribeiro, J. Mol. Catal. A: Chem., 1999, 144, 207-220.
- 36 L. Jie, L. Changcheng, D. Zhijian and Z. Huidong, China Pet. Process. Petrochem. Technol., 2019, 21, 7-14.
- 37 V. Galvita, G. Siddiqi, P. Sun and A. T. Bell, J. Catal., 2010, 271, 209-219.
- 38 T. I. Korányi, Z. Vít, D. G. Poduval, R. Ryoo, H. S. Kim and E. J. M. Hensen, J. Catal., 2008, 253, 119-131.
- 39 Y. Dai, J. Gu, S. Tian, Y. Wu, J. Chen, F. Li, Y. Du, L. Peng, W. Ding and Y. Yang, J. Catal., 2020, 381, 482-492.
- 40 D.-H. Ha, L. M. Moreau, C. R. Bealing, H. Zhang, R. G. Hennig and R. D. Robinson, J. Mater. Chem., 2011, 21, 11498-11510.
- 41 F. H. Saadi, A. I. Carim, W. S. Drisdell, S. Gul, J. H. Baricuatro, J. Yano, M. P. Soriaga and N. S. Lewis, J. Am. Chem. Soc., 2017, 139, 12927-12930.
- 42 X. Lan, R. Pestman, E. J. M. Hensen and T. Weber, J. Catal., 2021, 403, 181-193, DOI: 10.1016/J.JCAT.2021.01.031.
- 43 R. G. Greenler, K. D. Burch, K. Kretzschmar, R. Klauser, A. M. Bradshaw and B. E. Hayden, Surf. Sci., 1985, 152-153, 338-345.
- 44 A. Lapidus, A. Krylova, V. Kazanskii, V. Borovkov, A. Zaitsev, J. Rathousky, A. Zukal and M. Jančálková, Appl. Catal., 1991, 73, 65-81.
- 45 A. Y. Khodakov, J. Lynch, D. Bazin, B. Rebours, N. Zanier, B. Moisson and P. Chaumette, J. Catal., 1997, 168, 16-25.
- 46 D. Song, J. Li and Q. Cai, J. Phys. Chem. C, 2007, 111, 18970-18979.
- 47 K. Sato, Y. Inoue, I. Kojima, E. Miyazaki and I. Yasumori, J. Chem. Soc., Faraday Trans. 1, 1984, 80, 841-850.
- 48 G. Kadinov, C. Bonev, S. Todorova and A. Palazov, J. Chem. Soc., Faraday Trans., 1998, 94, 3027-3031.

- 49 J. E. Bailie, H. Rochester and G. J. Hutchings, J. Chem. Soc., Faraday Trans., 1997, 93, 2331–2336.
- 50 S. Todorova, V. Zhelyazkov and G. Kadinov, *React. Kinet. Catal. Lett.*, 1996, 57, 105–110.
- 51 K. A. Layman and M. E. Bussell, *J. Phys. Chem. B*, 2004, **108**, 10930–10941.
- 52 A. Sampath and D. W. Flaherty, Catal. Sci. Technol., 2020, 10, 993–1005.
- 53 S. A. Chang, A. Sampath and D. W. Flaherty, *J. Phys. Chem. C*, 2020, **124**, 18070–18080.
- 54 Y. Wang, Y. Wang, S. Wang, X. Guo, S. M. Zhang, W. P. Huang and S. Wu, *Catal. Lett.*, 2009, **132**, 472–479.
- 55 H. Verbeek and W. M. H. Sachtler, *J. Catal.*, 1976, 42, 257–267.
- 56 J. A. Cecilia, A. Infantes-Molina, E. Rodríguez-Castellón and A. Jiménez-López, J. Hazard. Mater., 2013, 260, 167–175.
- 57 Y. Wang, F. Liu, H. Han, L. Xiao and W. Wu, *ChemistrySelect*, 2018, 3, 7926–7933.
- 58 M. M. Bhasin, J. H. McCain, B. V. Vora, T. Imai and P. R. Pujadó, *Appl. Catal.*, *A*, 2001, 221, 397–419.
- 59 C. R. Riley, A. De La Riva, I. L. Ibarra, A. K. Datye and S. S. Chou, *Appl. Catal.*, A, 2021, 624, 118309.

- 60 L. Liu, M. Lopez-Haro, C. W. Lopes, C. Li, P. Concepcion, L. Simonelli, J. J. Calvino and A. Corma, *Nat. Mater.*, 2019, 18, 866–873.
- 61 B. Zhang, L. Zheng, Z. Zhai, G. Li and G. Liu, ACS Appl. Mater. Interfaces, 2021, 13, 16259–16266.
- 62 H. N. Pham, J. J. H. B. Sattler, B. M. Weckhuysen and A. K. Datye, ACS Catal., 2016, 6, 2257–2264.
- 63 L. Liwu, Z. Tao, Z. Jingling and X. Zhusheng, *Appl. Catal.*, 1990, **67**, 11–23.
- 64 B. K. Vu, M. B. Song, I. Y. Ahn, Y. W. Suh, D. J. Suh, W. Il Kim, H. L. Koh, Y. G. Choi and E. W. Shin, *Catal. Today*, 2011, 164, 214–220.
- 65 J. McGregor, Z. Huang, E. P. J. Parrott, J. A. Zeitler, K. L. Nguyen, J. M. Rawson, A. Carley, T. W. Hansen, J. P. Tessonnier, D. S. Su, D. Teschner, E. M. Vass, A. Knop-Gericke, R. Schlögl and L. F. Gladden, *J. Catal.*, 2010, 269, 329–339.
- 66 Z. Maeno, S. Yasumura, X. Wu, M. Huang, C. Liu, T. Toyao and K.-I. Shimizu, J. Am. Chem. Soc., 2020, 142, 4820–4832.
- 67 N. J. Escorcia, N. J. Libretto, J. T. Miller and C. W. Li, ACS Catal., 2020, 10, 9813–9823.